# Semiclassical coupled wave packet study of the nonadiabatic collisions Ar+(J)+H2: Zero angular momentum case

F. Aguillon, M. Sizun, V. Sidis, G. D. Billing, and N. Marković

---

**Articles you may be interested in**

Collinear (He,HD+) and (He,DH+) collisions: Transition state resonances and dynamics by timedependent quantal wave packet approach
J. Chem. Phys. **105**, 10934 (1996); 10.1063/1.472863

High resolution infrared spectra of H2–Ar, HD–Ar, and D2–Ar van der Waals complexes between 160 and 8620 cm−1
J. Chem. Phys. **105**, 2628 (1996); 10.1063/1.472158

A reliable new potential energy surface for H2–Ar
J. Chem. Phys. **105**, 2639 (1996); 10.1063/1.472127

Quantum mechanical angular distributions for the F+H2 reaction
J. Chem. Phys. **104**, 6531 (1996); 10.1063/1.471373

Experimental and theoretical study of H+HI→H2+I reaction dynamics at 1.3 eV collision energy
J. Chem. Phys. **96**, 2756 (1992); 10.1063/1.462024

---

# Semiclassical coupled wave packet study of the nonadiabatic collisions Ar⁺(J)+H₂: Zero angular momentum case

F. Aguillon, M. Sizun, and V. Sidis
*Laboratoire des Collisions Atomiques et Moléculaires, URA du CNRS No. 281, Bât. 351,*
*Université Paris XI, 91405 Orsay Cedex, France*

G. D. Billing
*Department of Chemistry, H. C. Ørsted Institute, University of Copenhagen, DK-2100 Copenhagen Ø,*
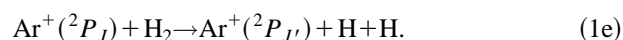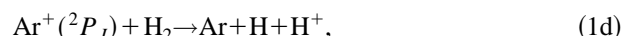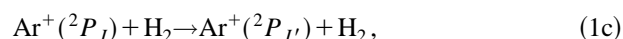*Denmark*

N. Marković
*Department of Physical Chemistry, University of Göteborg, S-41296 Göteborg, Sweden*

The title reaction is investigated for total angular momentum $\mathscr{J}=0$ using a semiclassical coupled wave packet method where the Smith–Whitten-type hyperspherical angles $\theta$ and $\varphi$ are treated quantally, and the hyperspherical radius $\rho$ is treated classically. The wave function is expanded over an electronic basis set which includes 28 states. The diabatic potential energy surfaces are determined by DIMZO calculations. Probabilities for reaction, charge transfer, collision induced dissociation, dissociative charge transfer, and fine structure transitions are obtained in the energy range $0.3 \text{ eV} \leq E \leq 30 \text{ eV}$. A comprehensive analysis of the reaction mechanisms is presented. © *1996 American Institute of Physics.* [S0021-9606(96)01811-6]

## I. INTRODUCTION

The collision between an $Ar^+(^2P_J)$ ion and a $H_2$ molecule may give rise to a number of processes,

$$Ar^+(^2P_J) + H_2 \rightarrow ArH^+ + H, \tag{1a}$$

$$Ar^+(^2P_J) + H_2 \rightarrow Ar + H_2^+, \tag{1b}$$

$$Ar^+(^2P_J) + H_2 \rightarrow Ar^+(^2P_{J'}) + H_2, \tag{1c}$$

$$Ar^+(^2P_J) + H_2 \rightarrow Ar + H + H^+, \tag{1d}$$

$$Ar^+(^2P_J) + H_2 \rightarrow Ar^+(^2P_{J'}) + H + H. \tag{1e}$$

All these processes are controlled by *nonadiabatic transitions* between the initial $Ar^+ + H_2$ state and the charge exchange state $Ar + H_2^+$. This is obvious for reactions (1b) and (1d). It is also the case for reaction (1a), because $ArH^+ + H$ does not correlate with the ground state reactants (Fig. 1). This is also the case for reactions (1c) and (1e) since the coupling induced by $H_2$ between the spin–orbit states of $Ar^+$ is much too weak to give rise to any significant direct fine structure transitions. This nonadiabatic character and the competition between channels (1a) to (1e) is probably the reason for the considerable interest this collisional system is attracting since more than 30 years.

Since the first determination of the cross section for reaction (1a),[1] a large number of experimental works (see Refs. 2–4 and references therein) have been devoted to this system. Among these, state selected experiments[3–12] have shown that the spin–orbit structure of the $Ar^+$ ion plays an important role; the reaction cross section (1a) is larger for $Ar^+(^2P_{1/2})$ than for $Ar^+(^2P_{3/2})$ by a factor $\sigma(1/2)/\sigma(3/2)$ lying between 1.3 and 2. They have also shown that the ratio between the charge transfer cross sections (1b) for $Ar^+(^2P_{1/2})$ and $Ar^+(^2P_{3/2})$ is even more favorable to $Ar^+(^2P_{1/2})$. This

has been understood as being due to the very close resonance between the $Ar^+(^2P_{1/2}) + H_2(v=0)$ and the $Ar + H_2^+(v=2)$ states which makes the charge transfer efficient at very large impact parameter for the $^2P_{1/2}$ state.

Many theoretical studies have accompanied the above experimental works.[6(b),12(c),13–26] Only two of these perform 3D dynamical calculations including the reaction channel (1a); the trajectory surface hopping (TSH) calculation of Chapman *et al.*,[18] and the calculation of Baer *et al.*,[22] based on the reactive infinite order sudden approximation. In these two approaches, the spin–orbit effect was neglected. Because capture models provided good estimations of the reaction cross section,[17] a number of works focused their attention on the entrance channel. Based on this idea, TSH calculations of Tanaka *et al.*[6(b)] have determined the energy dependence of spin–orbit resolved reaction cross sections. These results have been improved by Baer *et al.*,[24] who proposed another implementation of the reactive infinite order approximation; they assume that as soon as the system enters the $ArH^+ + H$ valley the reaction takes place. Accordingly, they performed their calculations in the entrance valley only by setting an absorbing negative imaginary potential at the entrance of the reaction valley. Yet this method does not provide any information on the internal states of the reaction products (1a). Moreover, inasmuch as it is based on a finite vibronic expansion, it cannot handle the dissociative processes (1d) and (1e).

The diatomics in molecule with zero overlap (DIMZO) potential energy surfaces of Kuntz *et al.*[16] have been used in calculations requiring the knowledge of the potential in the whole space.[18,22,24] These surfaces do not take into account the polarization interaction, and thus become questionable at low energy. However, we have used these surfaces in order to be in a position to compare with previous works.
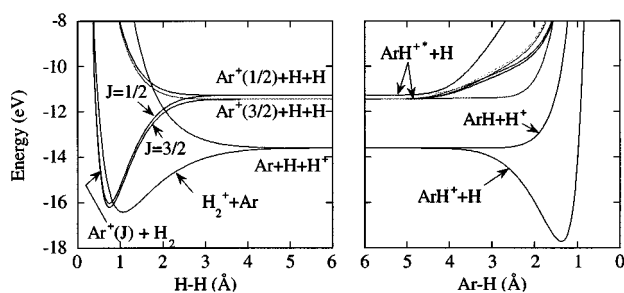
FIG. 1. Asymptotic potential energy curves of the ArH$_2^+$ system.



FIG. 2. Definition of the Jacobi coordinates $r_c$, $R_c$, and $\eta_c$ in the three rearrangement channels $c$. For sake of clarity, the argon atom is made lighter on the figure than it actually is.

The method used in this paper, first introduced by Billing and co-workers,[27] is based on a hyperspherical semiclassical approximation; the hyperspherical radius $\rho$ is treated classically, and the other nuclear degrees of freedom are treated quantally using a numerical description over a grid. The use of this technique has three main advantages.

(1) The nonadiabatic transitions are treated explicitly. Transitions due to motions which are handled quantally are treated exactly. Transitions due to motions that are handled classically obey quantal time dependent equations, the time dependence of the Hamiltonian arising from its dependence upon $\rho(t)$;

(2) The nonreactive, reactive, and dissociative channels are treated on the same footing. State to state information is obtained for each of the reactions (1a) to (1e);

(3) The time dependent treatment provides a sensible picture of the reaction, allowing one to visualize the intimate collision mechanisms, and to extract simple models that help to understand what happens during the collision.

The present work is mostly concerned with the collisions where both the total angular momentum $\mathscr{T}$ and the H$_2$ rotational angular momentum $j$ are zero. Only a few results obtained with $\mathscr{T}>0$ will be presented here. Section II presents the dynamical equations, Sec. III the asymptotic limit of the transformations between Jacobi and hyperspherical coordinates. In Sec. IV we present the derivation of the potential energy matrix. Section V is devoted to technicalities. The results are presented in Sec. VI, and discussed in Sec. VII.

## II. EQUATIONS OF MOTION

We use here a slightly modified version[27] of Johnson's hyperspherical coordinates.[28] Three Euler angles $\alpha$, $\beta$, and $\gamma$ define the orientation of the triatomic plane; the triatomic triangle is described by the hyperspherical radius $\rho$ and two hyperangles $\theta$ and $\varphi$. In a given arrangement channel $c$, the relationships between the hyperspherical coordinates and Jacobi coordinates $r_c$, $R_c$, and $\eta_c \in [0, \pi]$ are[28(a),29] (Fig. 2)

$$\frac{r_c^2}{d_c^2} = \frac{\rho^2}{2} [1 - \sin \theta \cos(\varphi - \varphi_c)], \tag{2a}$$

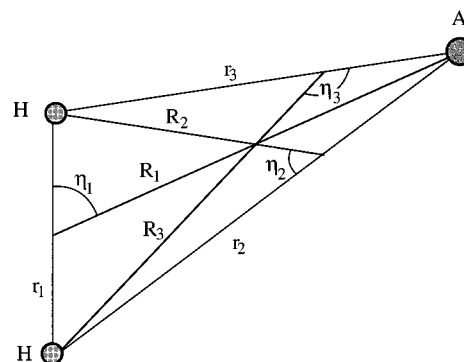$$d_c^2 R_c^2 = \frac{\rho^2}{2} [1 + \sin \theta \cos(\varphi - \varphi_c)], \tag{2b}$$

$$\cos \eta_c = \frac{\sin \theta \sin(\varphi - \varphi_c)}{\sqrt{1 - \sin^2 \theta \cos^2(\varphi - \varphi_c)}}. \tag{2c}$$

In the following, the channel $c = 1$ will refer to the Ar+H$_2$ channel, and channels $c = 2$ and $c = 3$ to the two ArH+H channels. $d_c$ and $\varphi_c$ depend only on the mass $m_1$ of the argon atom, and $m_2$ and $m_3$ of the H atoms,

$$d_c = \sqrt{\frac{m_c}{\mu} \left(1 - \frac{m_c}{m_1 + m_2 + m_3}\right)} \tag{3a}$$

and

$$\varphi_1 = \pi, \quad \varphi_2 = \pi + 2 \tan^{-1}\left(\frac{m_3}{\mu}\right),$$

$$\varphi_3 = \pi - 2 \tan^{-1}\left(\frac{m_2}{\mu}\right). \tag{3b}$$

$\mu$ is the hyperspherical reduced mass,

$$\mu = \sqrt{\frac{m_1 m_2 m_3}{m_1 + m_2 + m_3}}. \tag{4}$$

When the total angular momentum $\mathscr{T}$ equals 0, the wave function does not depend on the Euler angles $\alpha, \beta$, and $\gamma$. Here it is described in a semiclassical framework,[27] where the hyperspherical radius $\rho$ is treated classically whereas the hyperspherical angles $\theta$ and $\varphi$ are treated quantally. More precisely, the wave function $\Xi(r_{el}, \theta, \varphi; \rho)$ depends on the electronic coordinates denoted collectively by $r_{el}$, on the nuclear coordinates $\theta$ and $\varphi$, and parametrically on the classical quantity $\rho$. We define a transformed wave function $\Phi$, which is expanded over a diabatic electronic basis set $\zeta_n$ according to

$$\Phi(r_{el}, \theta, \varphi; \rho) = \sqrt{\frac{\rho^5 \sin \theta \cos \theta}{8}} \Xi(r_{el}, \theta, \varphi; \rho)$$

$$= \sum_n \Psi_n(\theta, \varphi; \rho) \zeta_n(r_{el}; \theta, \varphi, \rho). \tag{5}$$

The normalization condition of this wave function is simply

$$\int_0^{2\pi} d\varphi \int_0^{\pi/2} d\theta \sum_n |\Psi_n(\theta,\varphi;\rho)|^2 = 1. \tag{6}$$

Its evolution is governed by the time dependent quantal Hamiltonian,

$$H_q = \frac{2P_\theta^2}{\mu\rho^2} + \frac{2P_\varphi^2}{\mu\rho^2 \sin^2\theta} + V(\theta,\varphi,\rho) + \Delta V(\theta,\rho). \tag{7}$$

In Eq. (7), $P_\theta$, $P_\varphi$, $V$, and $\Delta V$ are matrix operators in the $\{\zeta_n\}$ representation. As the $\zeta_n$ constitute a diabatic electronic basis set, matrix elements of the momentum operators $P_q$ can be written

$$\langle \zeta_m | P_q | \zeta_n \rangle = -i\hbar \delta_{mn} \frac{\partial}{\partial q}. \tag{8}$$

The extra potential matrix $\Delta V$, defined by

$$\begin{aligned} \Delta V_{mn}(\theta,\rho) &= \langle \zeta_m | \Delta V(\theta,\rho) | \zeta_n \rangle \\ &= -\frac{\hbar^2}{2\mu\rho^2} \left( \frac{1}{4} + \frac{4}{\sin^2 2\theta} \right) \delta_{mn} \end{aligned} \tag{9}$$

arises from the coordinate transformation,[28(c)] and is independent of the electronic state. It is added to the diabatic potential

$$V_{mn}(\theta,\varphi,\rho) = \langle \zeta_m | H_{el}(r_{el},\theta,\varphi,\rho) | \zeta_n \rangle, \tag{10}$$

where $H_{el}$ is the electronic Hamiltonian. In the above expressions, the integration is carried out over the electronic coordinates $r_{el}$. The time dependent Schrödinger equation leads to a system of coupled partial differential equations,

$$\begin{aligned} i\hbar \frac{\partial \Psi_m}{\partial t} &= \left( \frac{-2\hbar^2}{\mu\rho^2} \frac{\partial^2}{\partial\theta^2} + \frac{-2\hbar^2}{\mu\rho^2 \sin^2\theta} \frac{\partial^2}{\partial\varphi^2} + V_{mm} + \Delta V \right) \\ &\quad \times \Psi_m + \sum_{n\neq m} V_{mn} \Psi_n, \end{aligned} \tag{11}$$

which is solved simultaneously with the classical Hamilton's equations of motion for $\rho$ using the classical Hamiltonian,

$$H_{cl} = \frac{P_\rho^2}{2\mu} + \sum_{m,n} \langle \Psi_m | H_q | \Psi_n \rangle, \tag{12}$$

where the integration is carried out over the hyperspherical angles $\theta$ and $\varphi$.

## III. ASYMPTOTIC CONSIDERATIONS

In the asymptotic regions, the wave function of the system is not normally described in terms of hyperspherical wave functions. An asymptotic wave function is characterized by the electronic state $i$, as well as the quantum number $\mathcal{T}$ and $\mathcal{M}_{\mathcal{T}}$ associated, respectively, with the total angular momentum and its projection along a fixed direction, which are constants of motion. In our case, $\mathcal{T}=0$ and $\mathcal{M}_{\mathcal{T}}=0$. Unless the collision leads to complete dissociation, an asymptotic wave function will also be characterized by the arrangement channel $c$ (1 for Ar+H₂, 2 for ArH+H, 3 for H+ArH), the vibrational and rotational quantum numbers $\nu$ and $j$ of the diatomic molecule, and the orbital angular momentum 1

TABLE I. Nonvanishing coefficients of the projections of the [Ar⁺+H₂(³Σ_u)] $(S,M_S,m_1)$ states as defined in text onto the Ar⁺$(J,M_J)$+H₂(³Σ_u,m_s) states for an $\Omega = |M_S + m_1| = |M_J + m_s|$ quantum number value of 5/2.

|  | $S=3/2$ $M_S=3\epsilon/2$ $m_1=\epsilon$ |
|---|---|
| $\Omega=5/2$ ($\epsilon=\pm1$) |  |
| $J=3/2$, $M_J=3\epsilon/2$, $m_s=\epsilon$ | 1 |

associated with the relative atom–molecule motion. In the asymptotic region, the semiclassical hyperspherical approximation amounts to a semiclassical approximation where the Jacobi coordinate $R_c$ is treated classically. Indeed, from Eqs. (2a) and (2b),

$$\rho = \sqrt{d_c^2 R_c^2 + \frac{r_c^2}{d_c^2}} \approx d_c R_c. \tag{13}$$

Then, in the $\mathcal{T}=0$ case, when the asymptotic wave function is characterized by the electronic state $i$, channel $c$, and diatomic quantum numbers $\nu$ and $j$, the asymptotic hyperspherical wave packet $\Psi_m$ associated with the electronic wave function $\zeta_m$ is[29]

$$\begin{aligned} \Psi_m(\theta,\varphi;\rho) &= (-1)^j \sqrt{\frac{\pi d_c^4}{2}} R_c \frac{g_\nu(r_c)}{\sqrt{r_c}} \sqrt{\sin \eta_c} \\ &\quad \times Y_{j0}(\eta_c,0) \delta_{im}, \end{aligned} \tag{14}$$

where $g_\nu(r_c)$ is the vibrational eigenstate $\nu$ of the diatomic molecule of channel $c$.

## IV. POTENTIAL ENERGY SURFACES AND COUPLINGS

The potential energy matrix $V(\theta,\varphi,\rho)$ is determined in three steps.

First, a DIMZO calculation similar to that of Kuntz *et al.*[16] is performed to compute the potential energy matrix regardless of the spin–orbit coupling. This step concerns eleven energy states correlated with

$$Ar(^1S) + H_2^+(^2\Sigma_g);$$

$$Ar^+(^2P_\alpha) + H_2(^1\Sigma_g), \quad \alpha=x,y,z;$$

$$Ar(^1S) + H_2^+(^2\Sigma_u);$$

$$Ar^+(^2P_\alpha) + H_2(^3\Sigma_u, m_s=0), \quad \alpha=x,y,z;$$

$$Ar^+(^2P_\alpha) + H_2(^3\Sigma_u, |m_s|=1), \quad \alpha=x,y,z,$$

where the $z$ axis joins the Ar atom and the center of mass of the H₂ molecule, and the $x$ axis is in the triatomic plane. $m_s$ is the projection of the H₂ electronic spin along the $z$ axis.

Second, the spin–orbit interaction is introduced in a way similar to the method proposed by Tully.[30] A first rotation transforms the Ar⁺($^2P_\alpha$) states into $(J,M_J)$ states. In this basis set, the diagonal spin–orbit matrix is added to the potential energy matrix. A second rotation transforms this basis

TABLE II. Same as Table I for $\Omega=3/2$.

| $\Omega=3/2$ ($\epsilon=\pm1$) | $S=3/2$ $M_S=3\epsilon/2$ $m_1=0$ | $S=3/2$ $M_S=\epsilon/2$ $m_1=\epsilon$ | $S=1/2$ $M_S=\epsilon/2$ $m_1=\epsilon$ |
|---|---|---|---|
| $J=3/2,\ M_J=3\epsilon/2,\ m_s=0$ | $0$ | $\sqrt{\dfrac{2}{3}}$ | $-\epsilon\sqrt{\dfrac{1}{3}}$ |
| $J=3/2,\ M_J=\epsilon/2,\ m_s=\epsilon$ | $\sqrt{\dfrac{2}{3}}$ | $\dfrac{1}{3}$ | $\epsilon\dfrac{\sqrt{2}}{3}$ |
| $J=1/2,\ M_J=\epsilon/2,\ m_s=\epsilon$ | $-\epsilon\sqrt{\dfrac{1}{3}}$ | $\epsilon\dfrac{\sqrt{2}}{3}$ | $\dfrac{2}{3}$ |

TABLE IV. Value of the coefficients $\epsilon(\mathscr{E},\mathscr{L},\mathscr{M})$ and $\epsilon'(\mathscr{E},\mathscr{L},\mathscr{M})$ introduced to symmetrize the electronic wave functions (see text).

| State | $\epsilon$ | $\epsilon'$ |
|---|---|---|
| $\mathrm{Ar}(^1S)+\mathrm{H}_2^+(^2\Sigma_g,\ m_s=\pm1/2)$ | $\mp1$ | $-1$ |
| $\mathrm{Ar}^+(J=3/2,\ M_J=\pm3/2)+\mathrm{H}_2(^1\Sigma_g)$ | $\pm1$ | $1$ |
| $\mathrm{Ar}^+(J=3/2,\ M_J=\pm1/2)+\mathrm{H}_2(^1\Sigma_g)$ | $\mp1$ | $-1$ |
| $\mathrm{Ar}^+(J=1/2,\ M_J=\pm1/2)+\mathrm{H}_2(^1\Sigma_g)$ | $\pm1$ | $-1$ |
| $\mathrm{Ar}(^1S)+\mathrm{H}_2^+(^2\Sigma_u,\ m_s=\pm1/2)$ | $\mp1$ | $1$ |
| $[\mathrm{Ar}^++\mathrm{H}_2(^3\Sigma_u)]\ (S=1/2,\ M_S=\pm1/2,\ m_1=\pm1)$ | $\pm1$ | $-1$ |
| $[\mathrm{Ar}^++\mathrm{H}_2(^3\Sigma_u)]\ (S=1/2,\ M_S=\pm1/2,\ m_1=0)$ | $\mp1$ | $1$ |
| $[\mathrm{Ar}^++\mathrm{H}_2(^3\Sigma_u)]\ (S=1/2,\ M_S=\pm1/2,\ m_1=\mp1)$ | $\pm1$ | $-1$ |
| $[\mathrm{Ar}^++\mathrm{H}_2(^3\Sigma_u)]\ (S=3/2,\ M_S=\pm3/2,\ m_1=\pm1)$ | $\pm1$ | $1$ |
| $[\mathrm{Ar}^++\mathrm{H}_2(^3\Sigma_u)]\ (S=3/2,\ M_S=\pm3/2,\ m_1=0)$ | $\mp1$ | $-1$ |
| $[\mathrm{Ar}^++\mathrm{H}_2(^3\Sigma_u)]\ (S=3/2,\ M_S=\pm3/2,\ m_1=\mp1)$ | $\pm1$ | $1$ |
| $[\mathrm{Ar}^++\mathrm{H}_2(^3\Sigma_u)]\ (S=3/2,\ M_S=\pm1/2,\ m_1=\pm1)$ | $\mp1$ | $-1$ |
| $[\mathrm{Ar}^++\mathrm{H}_2(^3\Sigma_u)]\ (S=3/2,\ M_S=\pm1/2,\ m_1=0)$ | $\pm1$ | $1$ |
| $[\mathrm{Ar}^++\mathrm{H}_2(^3\Sigma_u)]\ (S=3/2,\ M_S=\pm1/2,\ m_1=\mp1)$ | $\mp1$ | $-1$ |

set into spin eigenstates of $(\mathrm{ArH}_2)^+$, characterized by the values $S$ and $M_S$. This results in a total of 28 states, 10 of which have $S=1/2$ and are labeled as

$$\mathrm{Ar}(^1S)+\mathrm{H}_2^+(^2\Sigma_g,\ m_s);$$

$$\mathrm{Ar}^+(J,M_J)+\mathrm{H}_2(^1\Sigma_g);$$

$$\mathrm{Ar}(^1S)+\mathrm{H}_2^+(^2\Sigma_u,\ m_s).$$

The remaining 18 states are of the form

$$[\mathrm{Ar}^++\mathrm{H}_2(^3\Sigma_u)](S,M_S,m_1),$$

and split into 6 $S=1/2$ states and 12 $S=3/2$ states. $m_l$ denotes here the projection of the orbital quantum number of the $\mathrm{Ar}^+$ ion on the $z$ axis. The 18 $[\mathrm{Ar}^++\mathrm{H}_2(^3\Sigma_u)]$ $(S,M_S,m_1)$ states can be expressed in terms of the $\mathrm{Ar}^+(J,M_J)+\mathrm{H}_2(^3\Sigma_u,m_s)$ states according to the coefficients listed in Tables I–III.

Third, the above 28 states are symmetrized. For this purpose, let us call $|\mathscr{E},\mathscr{L},\mathscr{M}\rangle$ these states, where $\mathscr{L}$ and $\mathscr{M}$ denote collectively the angular momenta and their projections, and $\mathscr{E}$ all the other quantum numbers. The reflection $\sigma_v$ through the triatomic plane transforms $|\mathscr{E},\mathscr{L},\mathscr{M}\rangle$ into $\epsilon(\mathscr{E},\mathscr{L},\mathscr{M})|\mathscr{E},\mathscr{L},-\mathscr{M}\rangle$, where $\epsilon(\mathscr{E},\mathscr{L},-\mathscr{M})=-\epsilon(\mathscr{E},\mathscr{L},\mathscr{M})$ can have the value $+1$ or $-1$.[31] The particular values of the coefficients $\epsilon(\mathscr{E},\mathscr{L},\mathscr{M})$ are listed in Table IV. It follows that the two states defined by

$$\frac{1}{\sqrt{2}}\left(|\mathscr{E},\mathscr{L},\mathscr{M}\rangle+i\,\epsilon(\mathscr{E},\mathscr{L},\mathscr{M})|\mathscr{E},\mathscr{L},-\mathscr{M}\rangle\right)$$

and

$$\frac{1}{\sqrt{2}}\left(|\mathscr{E},\mathscr{L},\mathscr{M}\rangle-i\,\epsilon(\mathscr{E},\mathscr{L},\mathscr{M})|\mathscr{E},\mathscr{L},-\mathscr{M}\rangle\right),$$

are eigenstates of $\sigma_v$ with the eigenvalues $-i$ and $i$, respectively. Thus, in the basis set defined by the above transformation, the potential energy matrix can be written as

$$V=\begin{pmatrix} U & 0 \\ 0 & U^* \end{pmatrix}, \tag{15}$$

where $U$ is a $14\times14$ complex Hermitic matrix.

We can also take advantage of a second symmetry property, which is the rotation by $\pi$ around the $z$ axis $R_z(\pi)$. The effect of such a rotation is to transform the state

$$\frac{1}{\sqrt{2}}\left(|\mathscr{E},\mathscr{L},\mathscr{M}\rangle+i\,\epsilon(\mathscr{E},\mathscr{L},\mathscr{M})|\mathscr{E},\mathscr{L},-\mathscr{M}\rangle\right)$$

into the state

TABLE III. Same as Table I for $\Omega=1/2$.

| $\Omega=1/2$ ($\epsilon=\pm1$) | $S=3/2$ $M_S=3\epsilon/2$ $m_1=-\epsilon$ | $S=3/2$ $M_S=\epsilon/2$ $m_1=0$ | $S=3/2$ $M_S=-\epsilon/2$ $m_1=\epsilon$ | $S=1/2$ $M_S=\epsilon/2$ $m_1=0$ | $S=1/2$ $M_S=-\epsilon/2$ $m_1=\epsilon$ |
|---|---|---|---|---|---|
| $J=3/2,\ M_J=3\epsilon/2,\ m_s=-\epsilon$ | $0$ | $0$ | $\dfrac{1}{\sqrt{3}}$ | $0$ | $-\epsilon\sqrt{\dfrac{2}{3}}$ |
| $J=3/2,\ M_J=\epsilon/2,\ m_s=0$ | $0$ | $\dfrac{2}{3}$ | $\dfrac{\sqrt{2}}{3}$ | $-\epsilon\dfrac{\sqrt{2}}{3}$ | $\dfrac{\epsilon}{3}$ |
| $J=3/2,\ M_J=-\epsilon/2,\ m_s=\epsilon$ | $\sqrt{\dfrac{1}{3}}$ | $\dfrac{\sqrt{2}}{3}$ | $0$ | $\dfrac{2\epsilon}{3}$ | $0$ |
| $J=1/2,\ M_J=\epsilon/2,\ m_s=0$ | $0$ | $-\epsilon\dfrac{\sqrt{2}}{3}$ | $\dfrac{2\epsilon}{3}$ | $\dfrac{1}{3}$ | $\dfrac{\sqrt{2}}{3}$ |
| $J=1/2,\ M_J=-\epsilon/2,\ m_s=\epsilon$ | $-\epsilon\sqrt{\dfrac{2}{3}}$ | $\dfrac{\epsilon}{3}$ | $0$ | $\dfrac{\sqrt{2}}{3}$ | $0$ |

$$i\frac{\epsilon'(\mathcal{E},\mathcal{L},\mathcal{M})}{\sqrt{2}}(|\mathcal{E},\mathcal{L},\mathcal{M}\rangle - i\epsilon(\mathcal{E},\mathcal{L},\mathcal{M})|\mathcal{E},\mathcal{L},-\mathcal{M}\rangle)$$

corresponding to the symmetric position of the nuclei, i.e., with the hyperspherical angle $\varphi$ changed in $2\pi-\varphi$. The coefficients $\epsilon'(\mathcal{E},\mathcal{L},\mathcal{M})$ can be $+1$ or $-1$, and are listed in Table IV. Then, by multiplying the basis states defined in the previous step by $\sqrt{-\epsilon'(\mathcal{E},\mathcal{L},\mathcal{M})}$, we obtain the following property:

$$U(\theta,2\pi-\varphi,\rho)=U^*(\theta,\varphi,\rho). \tag{16}$$

The first 14 properly symmetrized states are

$$|\zeta_1\rangle=\frac{1}{\sqrt{2}}[\mathrm{ArH}_{2g}^+](|m_s=1/2\rangle-i|m_s=-1/2\rangle),$$

$$|\zeta_2\rangle=\frac{i}{\sqrt{2}}[\mathrm{Ar}^+\mathrm{H}_{2g}](|J=3/2,M_J=3/2\rangle$$
$$+i|J=3/2,M_J=-3/2\rangle),$$

$$|\zeta_3\rangle=\frac{1}{\sqrt{2}}[\mathrm{Ar}^+\mathrm{H}_{2g}](|J=3/2,M_J=1/2\rangle$$
$$-i|J=3/2,M_J=-1/2\rangle),$$

$$|\zeta_4\rangle=\frac{1}{\sqrt{2}}[\mathrm{Ar}^+\mathrm{H}_{2g}](|J=1/2,M_J=1/2\rangle+i|J=1/2,M_J$$
$$=-1/2\rangle),$$

$$|\zeta_5\rangle=\frac{i}{\sqrt{2}}[\mathrm{ArH}_{2u}^+](|m_s=1/2\rangle-i|m_s=-1/2\rangle),$$

$$|\zeta_6\rangle=\frac{1}{\sqrt{2}}[\mathrm{Ar}^+\mathrm{H}_2(^3\Sigma_u)](|S=1/2,M_S=1/2,m_l=1\rangle$$
$$+i|S=1/2,M_S=-1/2,m_l=-1\rangle),$$

$$|\zeta_7\rangle=\frac{i}{\sqrt{2}}[\mathrm{Ar}^+\mathrm{H}_2(^3\Sigma_u)](|S=1/2,M_S=1/2,m_l=0\rangle$$
$$-i|S=1/2,M_S=-1/2,m_l=0\rangle),$$

$$|\zeta_8\rangle=\frac{1}{\sqrt{2}}[\mathrm{Ar}^+\mathrm{H}_2(^3\Sigma_u)](|S=1/2,M_S=1/2,m_l=-1\rangle$$
$$+i|S=1/2,M_S=-1/2,m_l=1\rangle),$$

$$|\zeta_9\rangle=\frac{i}{\sqrt{2}}[\mathrm{Ar}^++\mathrm{H}_2(^3\Sigma_u)](|S=3/2,M_S=3/2,m_l=1\rangle$$
$$+i|S=3/2,M_S=-3/2,m_l=-1\rangle),$$

$$|\zeta_{10}\rangle=\frac{1}{\sqrt{2}}[\mathrm{Ar}^+\mathrm{H}_2(^3\Sigma_u)](|S=3/2,M_S=3/2,m_l=0\rangle$$
$$-i|S=3/2,M_S=-3/2,m_l=0\rangle),$$

(17)

$$|\zeta_{11}\rangle=\frac{i}{\sqrt{2}}[\mathrm{Ar}^+\mathrm{H}_2(^3\Sigma_u)](|S=3/2,M_S=3/2,m_l=-1\rangle$$
$$+i|S=3/2,M_S=-3/2,m_l=1\rangle),$$

$$|\zeta_{12}\rangle=\frac{1}{\sqrt{2}}[\mathrm{Ar}^+\mathrm{H}_2(^3\Sigma_u)](|S=3/2,M_S=1/2,m_l=1\rangle$$
$$-i|S=3/2,M_S=-1/2,m_l=-1\rangle),$$

$$|\zeta_{13}\rangle=\frac{i}{\sqrt{2}}[\mathrm{Ar}^+\mathrm{H}_2(^3\Sigma_u)](|S=3/2,M_S=1/2,m_l=0\rangle$$
$$+i|S=3/2,M_S=-1/2,m_l=0\rangle),$$

$$|\zeta_{14}\rangle=\frac{1}{\sqrt{2}}[\mathrm{Ar}^+\mathrm{H}_2(^3\Sigma_u)](|S=3/2,M_S=1/2,m_l=-1\rangle$$
$$-i|S=3/2,M_S=-1/2,m_l=1\rangle),$$

and the last 14 electronic states are given by

$$|\zeta_{i+14}\rangle=|\zeta_i\rangle^*. \tag{18}$$

In the following, we shall refer to these electronic states by a simplified notation, e.g., $\mathrm{Ar}^+(3/2,3/2)+\mathrm{H}_{2g}$ for $\zeta_2$.

An important consequence of Eq. (16) is that it is not necessary to consider all six $\mathrm{Ar}^+(J,M_J)+\mathrm{H}_{2g}$ initial electronic states for the dynamics calculation. The results for the entrance states $|\zeta_{16}\rangle$, $|\zeta_{17}\rangle$, and $|\zeta_{18}\rangle$ can be deduced from those obtained for $|\zeta_2\rangle$, $|\zeta_3\rangle$, $|\zeta_4\rangle$. Indeed, if two systems are prepared in two states such that their classical variables satisfy

$$\rho'=\rho, \quad P'_\rho=P_\rho \tag{19}$$

and their wave functions satisfy

$$\Psi'_{n'}(\theta,\varphi)=\Psi_n(\theta,2\pi-\varphi)$$
$$\text{with }\begin{cases} n'=n+14 & 1\le n\le 14 \\ n'=n-14 & 15\le n\le 28 \end{cases} \tag{20}$$

then one can see by introducing Eqs. (15) and (16) into Eqs. (11) and (12) that the properties of Eqs. (19) and (20) remain true throughout the collision.[32] As a consequence, two $\mathrm{Ar}^+(J,M_J)+\mathrm{H}_{2g}(v,j=0)$ collisions with initial electronic state $n$ or $n+14$ will lead to identical results.

In conclusion, for each value of the collision energy, the symmetry properties reduce the problem to the study of three collisions involving 14 coupled wave packets (instead of six collisions involving 28 coupled wave packets).

## V. IMPLEMENTATION

Each of the coupled wave packets $\Psi_n(\theta,\varphi;\rho)$ is represented on an equally spaced rectangular mesh, having 256 points in $\varphi$ and 64 points in $\theta$. The initial wave packet is prepared according to Eq. (14). The initial value of $\rho$ is 10 Å, and the initial value of $p_\rho$ is such that

$$p_\rho=-\sqrt{2\mu E_{\mathrm{coll}}}, \tag{21}$$
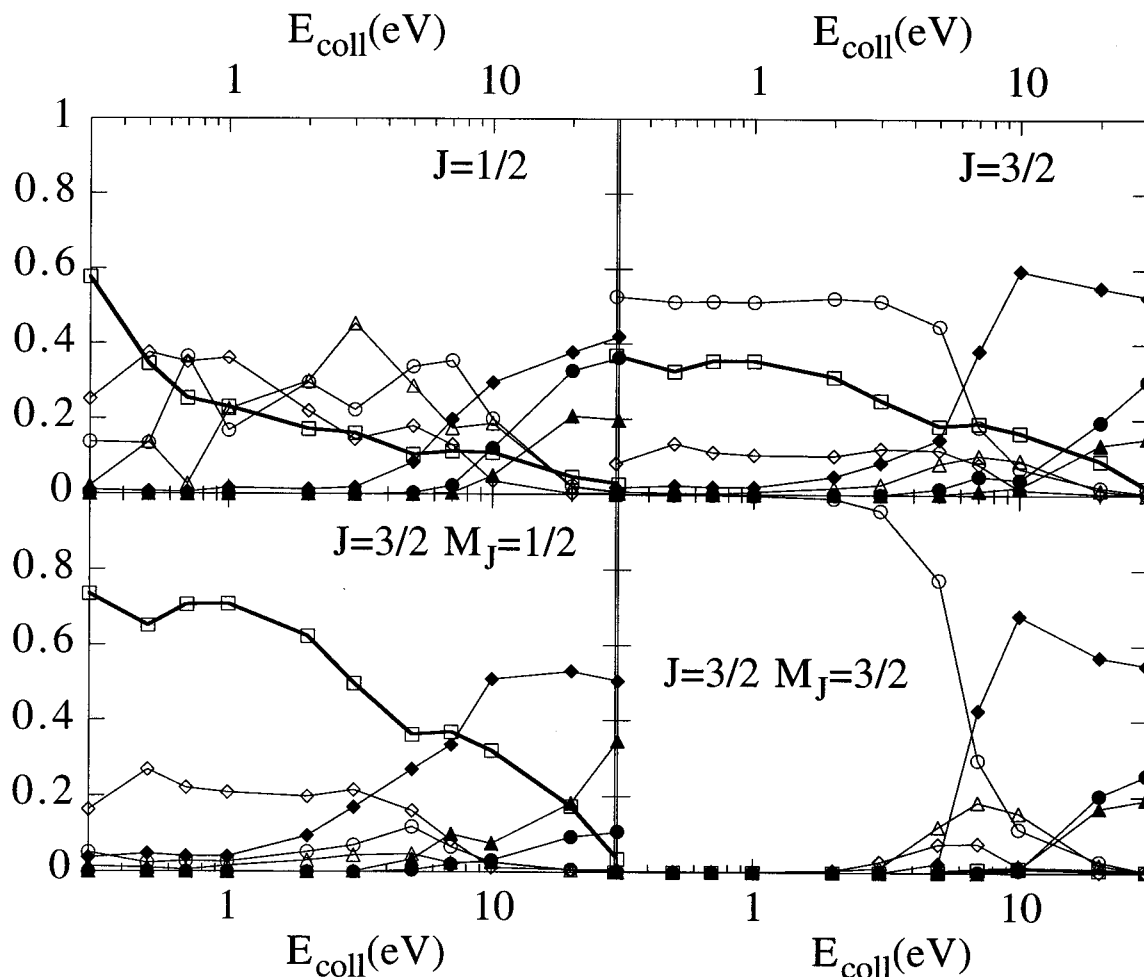
FIG. 3. Energy dependence of the probabilities for the Ar$^+$($J$)+H$_2$ collision to populate the different channels. Open circles, Ar$^+$($J'$=3/2)+H$_2$; open triangles, Ar$^+$($J'$=1/2)+H$_2$; open diamonds, Ar+H$_2^+$; open squares, ArH$^+$+H; full circles, Ar$^+$($J'$=3/2)+H+H; full triangles, Ar$^+$($J'$=1/2)+H+H; full diamonds, Ar+H+H$^+$. The upper left frame refers to the $J$=1/2 initial state of the Ar$^+$ ion, the upper right one to the $J$=3/2 initial state of the Ar$^+$ ion. The latter result is obtained from an equal mixing of the $M_J$=1/2 state, whose results are shown in the lower left frame, and of the $M_J$=3/2 state, whose results are shown in the lower right frame.

where $E_{coll}$ is the center of mass collision energy.

In order to integrate the time dependent Schrödinger equation, the evaluation of the quantal Hamiltonian makes use of the FFT technique.[33] As the wave packets must be zero for both $\theta$=0 and $\theta$=$\pi$/2 [Eq. (5)], a sine Fourier transform is used for the $\theta$ coordinate. It is not necessary to determine the time evolution of the wave packets for $\theta$=0 and $\theta$=$\pi$/2; we thus do not have any trouble with the singularities of $H_q$ and $\Delta V$ at these points. However, large values of the potential $V+\Delta V$ make the numerical calculations unstable. This difficulty has been overcome by limiting the value of the potential to a fixed value in the strongly forbidden classical regions, where the wave packets never go. The same type of instabilities also arise at small values of $\theta$ because of the $p_\varphi^2/\sin^2\theta$ term in Eq. (7). To get rid of this problem, we first perform the FFT in $\varphi$ only. In the resulting $\theta$, $p_\varphi$ representation of the wave packets, we evaluate the purely local $p_\varphi^2/\sin^2\theta$ term that we limit in the strongly forbidden classical regions. We then perform a FFT in $\theta$ only, in order to evaluate the first term of Eq. (7).

The time dependent Schrödinger equation is solved using the short iterative Lanczos algorithm.[34] Ten Lanczos vectors are computed. The time step is fixed by the condition that the contribution of the last Lanczos vector to the propagated wave packet is smaller than $2\times10^{-4}$. However, it is bound to be less than 0.15 fs to keep a good accuracy in the integration of the classical motion. Typically, this limitation comes into play during 2/3 of the collision time, in the asymptotic regions. In the inner zone, the time step decreases down to typically 0.05 fs.

At the end of the collision, the wave packet is analyzed. When state to state information is not required, a rough analysis is performed by defining three rectangular zones[27(c)] of the grid $(\theta,\varphi)$:$0<\theta<\pi/2$ and $0<\varphi<(\varphi_1+\varphi_3)/2$ corresponds to one ArH+H channel; $0<\theta<\pi/2$ and $(\varphi_1+\varphi_2)/2<\varphi<2\pi$ to the other ArH+H channel; $0<\theta<\pi/2$ and $(\varphi_1+\varphi_3)/2<\varphi<(\varphi_1+\varphi_2)/2$ to the Ar+H$_2$ channel [the $\varphi_i$ are defined in Eq. 3(b)]. The probability for each electronic state in each channel is determined by integrating the $|\Psi_n(\theta,\varphi;\rho)|^2$ probability density over the hyperspherical
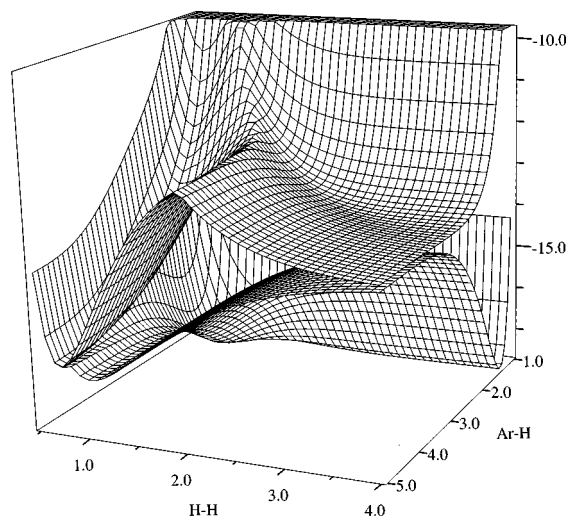
FIG. 4. Adiabatic DIMZO potential energy surfaces of the ArH$_2^+$ system in collinear geometry. Energy is in eV, distances in Å.

angles $\theta$ and $\varphi$. Actually, as the diabatic basis is relevant in the Ar+H$_2$ arrangement and the adiabatic basis set is relevant in the ArH+H channels, an electronic basis change has to be performed in the two rectangular zones located around $\varphi_2$ and $\varphi_3$ before the integration. When state-to-state probabilities are required, the final wave packets are analyzed by projection onto asymptotic rovibrational wave functions constructed from Eq. (14).

In order to save computer time, we have performed most of the calculations by taking into account the eight $S$=1/2 electronic states only. That the quartet states can be dropped has been checked by making three calculations with the fourteen doublet+quartet electronic states at three collision energies. The agreement between the eight states and the fourteen states calculations is very good; the total population of the quartet states never exceeds 1% at 30 eV, 0.1% at 3 eV, and 0.01% at 0.3 eV.

## VI. RESULTS

Figure 3 shows the energy dependence of the probability of finding the system in the different states at the end of the collision. Calculations have been carried out for all three
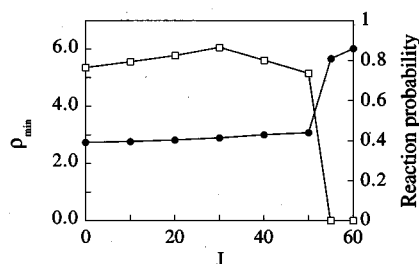


FIG. 5. Distance of closest approach in Å (full circles) and reaction probability (open squares) for a collision starting from the $J$=3/2 $M_J$=1/2 state with a collision energy $E$=0.3 eV, and various values of the total angular momentum $\mathscr{J}$.

Ar$^+$($J$,$M_J$)+H$_2$ states over the energy range 0.3–30.0 eV. At high collision energy, the system completely dissociates whatever its initial state is. At low and intermediate energy, the three initial electronic states do not lead to the same behavior; the $J$=3/2 $M_J$=3/2 state is almost inert. This nonreactivity is simply related to the fact that (i) the charge exchange process is the first step of the reaction (Figs. 1 and 4) and (ii) this electronic state is not coupled with the charge exchange state in the entrance channel. The two $M_J$=1/2 states are reactive, mainly at low energy, and they both give rise to charge exchange. However, their behavior is not identical, especially at intermediate energy, where the $J$=3/2 $M_J$=1/2 is more reactive, despite of the very close resonance ($\Delta E$=16 meV) between the Ar$^+$($J$=1/2,$M_J$=1/2)+H$_2$($v$=0) and the Ar+H$_2^+$($v$=2) states.

Although this paper is specialized in the detailed study of the $\mathscr{J}$=0 case, a few comparisons can be made with previously published results. Considering the reactive channel (1a), Baer *et al.*[24] reported a $\mathscr{J}$=0 reaction probability of about 0.37 for the $J$=3/2 fine structure state of Ar$^+$ at a collision energy of 1.289 eV; by linearly interpolating between our results obtained at collision energies of 1 and 2 eV, we find a reaction probability of 0.34 for the same $J$=3/2 initial Ar$^+$ state. The latter is due to a reaction probability of 0.68 for the $J$=3/2 $M_J$=1/2 state, and a reaction probability less than $10^{-4}$ for the $J$=3/2 $M_J$=3/2 state. The agreement is not as good for the $J$=1/2 fine structure state; at a collision energy of 0.946 eV, we find a reaction probability of 0.25, much lower than the probability of 0.61 found by Baer *et al.*[24] As these two calculations use the same potential energy surfaces, the difference can only be due to the approximations done in the dynamical treatment. In order the check to what extent the common trajectory assumption made in the semiclassical approximation could explain the difference between the two $J$=1/2 results, we have tested the sensitivity of our calculation with respect to the choice of this common trajectory. This has been done by requiring the classical $\rho$ motion in the $J$=1/2 case to be the same as that for the $J$=3/2 $M_J$=1/2 case at the same collision energy. In such conditions, the reaction probability at 0.946 eV reaches 0.32 instead of 0.25. Thus the discrepancy between the present semiclassical results and the IOS calculation can probably not be attributed only to the common trajectory approximation. Yet its origin is still not clear. A closer comparison with previously published results concerning the reaction (1a) can also be done by looking at preliminary calculations for nonzero total angular momentum $\mathscr{J}$ obtained in the following conditions: Ar$^+$($J$=3/2,$M_J$=1/2)+H$_2$($v$=0,$j$=0) at a collision energy $E_{coll}$=0.3 eV. A first qualitative comparison is the shape of the opacity function (Fig. 5) corresponding to the formation of the ArH$^+$ion; as already observed by Baer *et al.*[22,24] and by Chapman,[18(b)] this opacity function does not present any structure. Assuming that no reaction occurs at all in the $J$=3/2 $M_J$=3/2 case, the cross section obtained for a statistical mixing of the Zeeman substates of Ar$^+$($J$=3/2) is 12 Å$^2$, which fits nicely with the theoretical cross sections linearly interpolated from Ref. 24 (12.1 Å$^2$) or Ref. 18(b) (12.3 Å$^2$); however, it is significantly lower than the experi-
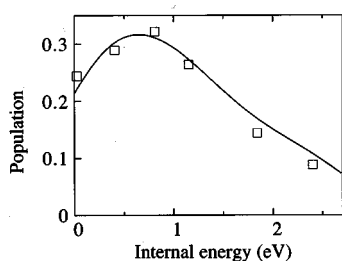
FIG. 6. Internal energy distribution of the H$_2^+$ ions formed by charge exchange between a statistical mixing of Ar$^+(^2P_J)$ and a H$_2$ molecule. The origin of the internal energy is H$_2^+(v=0, j=0)$. Squares, experimental data of Ref. 37 at a collision energy $E_{coll}=3.44$ eV. Solid line, present work, after proper convolution to simulate the finite experimental resolution, at $E_{coll}=3$ eV.



FIG. 7. Schematic flowchart of the collision. The behavior of the system is diabatic only in the asymptotic region and in the Ar+H$_2$ channel. On the reaction coordinate axis, the three letters $A$, $B$, and $C$ denote the regions which play a crucial role in the dynamics of the collision.

mental cross sections measured by Tanaka *et al.*[6] (27 Å$^2$) and by Liao *et al.*[3(b)] (23 Å$^2$). This mismatch between three very different dynamical calculations and two experiments could be related to the potential energy surfaces. The last comparison we can make for the reactive process is the internal state distribution of the ArH$^+$ product molecule. Gilibert *et al.*[35] have obtained state to state cross sections in a 3D quantal calculation of the reaction Ar+H$_2^+(v=0,j=0)$ →ArH$^+(v,j)$+H, for a collision energy of 0.06 eV. Their result cannot be closely compared to ours. First, the initial state is not the same in both cases. Second, it is well known that the semiclassical approximation leads to a population of energetically closed channels;[36] in our case, this drawback makes the internal state distribution unreliable at collision energies below about 1 eV. Nevertheless, the internal state distributions we observe at higher energy tend to go along the main conclusions of Ref. 35, i.e., we do not generally observe any inversion in the vibrational distribution, and high rotational excitation is produced by the reaction. Still, our vibrational distributions are generally not as smooth as those of Ref. 35, and, unlike the results reported there, our rotational populations are not peaked at their maximum $j$ value.

Considering the charge transfer channel (1b), we can compare our results with probabilities obtained at low $\mathscr{J}$ values in Ref. 24. According to these results, the charge exchange probability is roughly 1/3 of the reaction probability both for $J=1/2$ at $E_{coll}=0.946$ eV and for $J=3/2$ at $E_{coll}=1.289$ eV. This leads to a charge transfer probability for $\mathscr{J}=0$ estimated to about 0.20 for $J=1/2$ at 0.946 eV, and to about 0.12 for $J=3/2$ at 1.289 eV. In our calculation, we find a probability of 0.40 in the first case, and 0.10 in the second one. Just as for the reaction probabilities, the agreement between the IOS calculation and the present semiclassical calculation is nice for the $J=3/2$ initial fine structure state. The discrepancy is also clear for the $J=1/2$ initial state, but as mentioned above the reason for this discrepancy is still puzzling. A direct comparison with experimental data can also be done. Indeed, Hierl *et al.*[37] have demonstrated the existence at large scattering angle of an intimate collision mechanism for the charge transfer, which has been confirmed
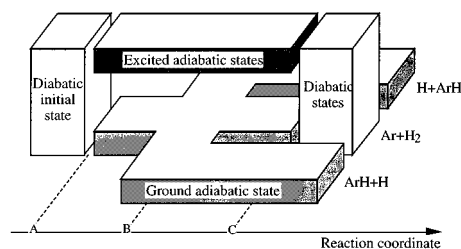
theoretically.[24] From their measurement of the product translational energy of the H$_2^+$ ion, one can deduce the internal energy distribution. Thus, it has been possible to compare their data with our theoretical internal state distribution, provided the following assumptions are made: (i) our $\mathscr{J}=0$ results are representative of this intimate charge transfer mechanism; (ii) the initial rotation of the H$_2$ molecule does not play any crucial role, so that our $j=0$ results are representative of the thermally populated molecules in the experiment. The result of this comparison, after proper convolution of the theoretical data in order to simulate the experimental resolution, is shown on Fig. 6. Yet, taking into account the number of assumptions done to obtain this result, the very nice agreement of Fig. 6 should not be overemphasized.

For reaction (1c), we note in our results that the $J=3/2→J=1/2$ reaction probability is much weaker than the $J=1/2→J=3/2$ one. The same trend is observed in the cross sections, either obtained from theory[24] of from experiments.[3(b),38] Finally, we find a very large dissociation probability at high energy [reactions 1(d) and 1(e)]. This leads in particular to a ratio H$^+$/H$_2^+$ which differs by orders of magnitude from the corresponding cross sections ratio as observed by Liao *et al.*[3(b)] This is but an apparent discrepancy; the $\mathscr{J}=j=0$ case studied here corresponds to head-on collisions, which at high energy can barely produce anything but complete dissociation. As soon as the total angular momentum increases, the dissociation probability is likely to vanish, as predicted by Chapman,[18(b)] thereby leading to a small dissociative charge exchange cross section.

## VII. INTERPRETATION AND DISCUSSION

Although the calculations have been performed in the diabatic basis set, the interpretation of the results often requires the use of both diabatic and adiabatic pictures. Indeed, the diabatic character of our electronic states is ensured by the fact that each state is described by the same combination of atomic orbitals irrespective of the nuclear geometry. Thus diabatic states which preserve the *gerade* or *ungerade* character of H$_2$ orbitals cannot individually describe the ArH$^+$ product state where these characters are completely lost. On the other hand, the adiabatic picture is not relevant at all in the entrance channel, since the crossing of the Ar$^+$+H$_2$ and the Ar+H$_2^+$ states (Fig. 1) makes the Born–Oppenheimer
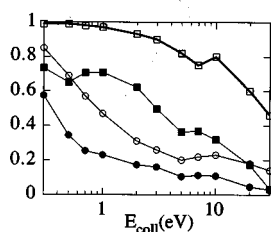
FIG. 8. Open symbols, energy dependence of the probability of finding the system on the adiabatic ground surface after the intermediate zone A for a given initial state of the Ar$^+$ ion. Full symbols, reaction probability for the same initial state. Squares and circles correspond to $J=3/2$ $M_J=1/2$ and $J=1/2$ $M_J=1/2$ initial states, respectively.

approximation break down. The subsequent question is to know when the behavior of the system flips from a diabatic to an adiabatic behavior as the collision proceeds. Part of the answer can be found in Fig. 4, which shows the two lowest adiabatic potential energy surfaces in collinear geometry. The energy gap between the ground state and the first excited states grows rapidly in the entrance channel up to a few eV. Thus, nonadiabatic coupling will barely induce transitions between the ground adiabatic surface and the excited surfaces except in the entrance channel, at relatively large intermolecular distances. The situation is not as simple for the adiabatic excited states which always stay energetically close to each other; nonadiabatic transitions between these excited states occur throughout the collision. However, none of these adiabatic excited states are reactive which greatly simplifies the understanding of the reaction dynamics. The collision can thus be roughly described using the flow chart of Fig. 7. The system behaves diabatically at the beginning of the collision, and then, when the coupling increases, it spreads over the ground adiabatic surface and the adiabatic excited surfaces (zone A on Fig. 7). The reaction only takes place in the inner region on the ground adiabatic surface (zone B). The part of the system that was adiabatically excited has to go back to the diabatic states in the Ar+H$_2$ channel (zone C). In the following, we will often make reference to these critical regions, especially zone A of Fig. 7, which will be referred to as the intermediate zone, and zone B, which will be referred to as the reaction zone.

Before going further in the presentation of the results and in their interpretation, let us stress some specifics of the presently investigated collision. The total angular momentum is $\mathscr{J}=0$, and the initial rotational quantum number of the H$_2$ molecule is $j=0$; classically speaking, this corresponds to a head on collision, which is a very particular event. The question then is to what extent the present results are representative of more general conditions. The answer lies in the shape of the potential energy surfaces; the reactive ground adiabatic surface does not present any activation barrier, and has a potential well that is deeper than 1 eV (Fig. 4). Unless the collision energy is much larger than the potential well depth, a system which evolves on this surface will have a short distance of closest approach as soon as it overcomes the centrifugal barrier. A preliminary calculation (Fig. 5) shows
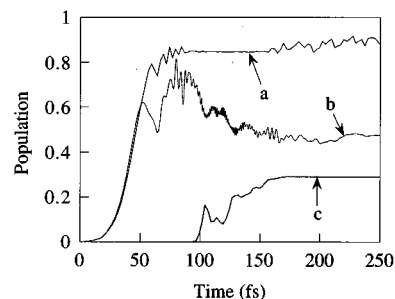


FIG. 9. Time evolution of the population of different states, as obtained in the following conditions: initial state Ar$^+$($J=3/2, M_J=1/2$), collision energy $E=0.3$ eV. Curve (a), population of the ground adiabatic state. Curve (b), population of the diabatic state correlated with the Ar+H$_2^+$($^2\Sigma_g$) state. Curve (c), population of the reactive channel of the adiabatic ground state.

that the hyperspherical distance $\rho$ of closest approach is almost constant over a large range of $\mathscr{J}$ values. Consequently, a $\mathscr{J}=0$ calculation is certainly representative of a wide range of low energy reactive collisions which necessarily occur on the ground adiabatic potential energy surface. Actually it is precisely at low energy that the reaction cross section is important, as shown by previous experiments and calculations [see e.g., Refs. 2 and 6(b)]. On the other hand, the present calculations are certainly not representative of what happens when the system evolves on the excited adiabatic surfaces, because these surfaces are repulsive. Then, in the following, although the method employed here treats on an equal footing the reactive, nonreactive and dissociative channels, we shall mainly focus on the reaction dynamics. The description of the collision then amounts to answering the following two questions:
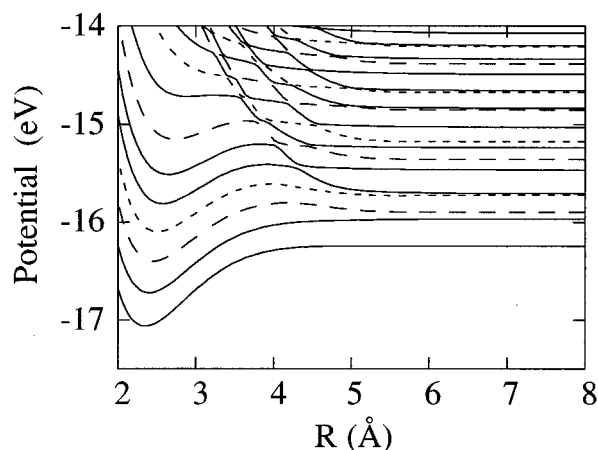


FIG. 10. Adiabatic vibronic network obtained in collinear configuration in the Jacobi set of coordinates corresponding to the entrance channel. The vibronic states are correlated at large $R$ distances to the Ar+H$_2^+$($^2\Sigma_g$) channel (full lines), the Ar$^+$($J=3/2$ $M=1/2$)+H$_2$ channel (long dashes), and to the Ar$^+$($J=1/2$ $M_J=1/2$)+H$_2$ channel (short dashes). At short distances, these adiabatic vibronic states are correlated to vibrational eigenstates of the electronic adiabatic states.
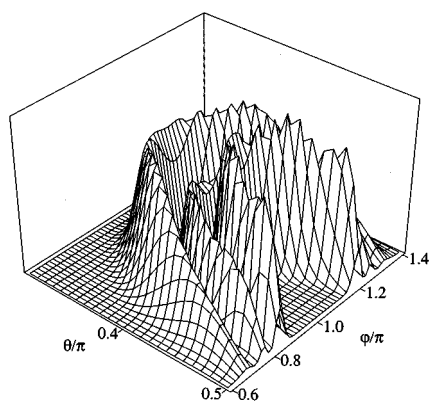
FIG. 11. Adiabatic ground state probability density. The collision starts at $\rho=10$ Å with a collision energy $E=0.3$ eV; the system is initially in the $Ar^+(J=3/2 \ M_J=1/2)+H_2(^1\Sigma_g)$ state. After 80 fs, it has reached the value $\rho=4.24$ Å, and the coupling between the diabatic electronic states is large, so that the behavior of the system is much easier to describe in the adiabatic electronic basis set. In the hyperspherical view used here, the point $r_{H-H}=0$ is found at $\theta=\pi/2$ and $\varphi=\pi$; along radial lines issued from this point, the $r_{H-H}$ distance increases, while the $H_2$ molecule does not rotate; conversely, along circles centered on the same point, the $H_2$ molecule rotates with a constant $r_{H-H}$ elongation. The radial structure shows that the system is in its $v=2$ vibrational level. The angular behavior also shows that the onset of the interaction is sudden with respect to the rotation; the system has almost the same probability density as the $j=0$ initial rotational level, since there is no angular structure. The decrease of the probability density along the $\theta=\pi/2$ axis is not related to any rotational structure, but to the fact that this axis corresponds to the collinear configurations, which are statistically less probable in the $j=0$ rotational state than perpendicular configurations localized near the $\varphi=\pi$ axis.

(i)   How does the system traverse the first intermediate zone A defined in Fig. 7?

(ii)  How does the reaction take place on the ground adiabatic surface in the reaction zone B, and how does the dynamics in this zone affect the reaction products?

These questions will be answered in the next two sections.

## A. Passing the intermediate zone

The way the system goes from its initial diabatic state to the intermediate adiabatic ground or excited state governs the reaction probability. This is shown by the strong correlation between the reaction probability and the probability for the system to be found in the ground adiabatic state (Fig. 8). One should emphasize that it is not possible to find such a correlation between the reaction probability and the probability for the system to undergo a charge exchange in the beginning of the collision (Fig. 9). Indeed, the system behaves very adiabatically in the inner region, which means that a large number of charge exchange transitions occur throughout the collision. That is the reason why the close resonance between the $Ar^+(J=1/2,v=0)+H_2$ and the $Ar+H_2^+(v=2)$ does not play any role in the reaction dynamics; this resonance makes it possible to undergo a first charge exchange transition at very large internuclear distance, but this is of little importance for the reaction since the system performs a large number of such transitions in the inner region. However, this resonance plays a crucial role for collisions occur-

ring at large impact parameters which prevent the system to get over the centrifugal barrier and reach the inner region. This resonance thus has a determinant influence on the charge exchange cross section.

The way in which the system passes the intermediate zone A can be qualitatively understood by considering separately the rotational motion of the $H_2$ molecule on one hand, and its vibronic behavior on the other hand. In the considered energy range, the branching time $T_{branch}$ of the coupling between the diabatic states (i.e., the time the system takes to go through the intermediate zone A) is always smaller than a rotational period $T_{rot}$ of the $H_2$ molecule. Consequently, the system is expected to keep the same probability density of $H_2$ orientations as in the initial $j=0$ state. In contrast to this sudden behavior vis-à-vis the rotation, the vibronic motion tends to be adiabatic at least at collision energies below a few eV. Then, the $H_2$ molecule tends to remain in the same adiabatic vibronic level when traversing the intermediate zone. One can then use the adiabatic vibronic network (Fig. 10) as a vibronic correlation diagram, since the adiabatic vibronic states are vibrational eigenstates of the diabatic electronic states at large $R$, and vibrational eigenstates of the adiabatic electronic states at small $R$. As an example, during a collision between $Ar^+(J=3/2,M_J=1/2)$ and $H_2$, the system remains in the third vibronic state (see Fig. 10). Then, it is expected to be found almost entirely in the $v=2$ level of the adiabatic ground state potential. This is exactly what is observed in the collision, as witnessed by Fig. 11, where the radial vibrational structure in the probability density is that of a $v=2$ level, while the lack of angular structure is a memory of the $j=0$ initial rotational level. Of course, this adiabatic vibronic behavior is not strict; as soon as dynamical couplings between two adiabatic vibronic states are of the same order as their energy separation, nonadiabatic transitions occur. For instance, nonadiabatic transitions occur even at very low energy between the $Ar^+(J=1/2)+H_2(v=0)$ and the $Ar+H_2^+(v=2)$ levels at large internuclear distances, because of the close resonance between these two states. Consequently, at low energy, a system prepared in the $Ar^+(J=1/2)+H_2(v=0)$ state is found after the transition zone A in a mixture of the $v=3$ and $v=4$ levels of the adiabatic ground state potential. However, as mentioned above, this resonance does not play any role in the choice of the electronic adiabatic state the system follows; it only changes the vibrational quantum number of the system by one unit.

In the general case, i.e., when the vibronic levels cannot be regarded as resonant, nonadiabatic transitions play a significant role at high energy, typically above a few eV. In such a situation, the adiabatic vibronic network can no more be used as a correlation diagram. One guideline to understand the behavior of the system in the few eV energy regime is the frozen wave packet approximation; the system follows the electronic adiabatic state it was originally in, without performing any vibrational motion.[39] For example, a system prepared in the $Ar^+(J=3/2,M_J=1/2)+H_2(v=0)$ state is initially in the adiabatic electronic ground state for $r_{H-H}<0.84$ Å and in the first adiabatic electronic excited state for $r_{H-H}>0.84$ Å (Fig. 1). According to the mentioned approxi-
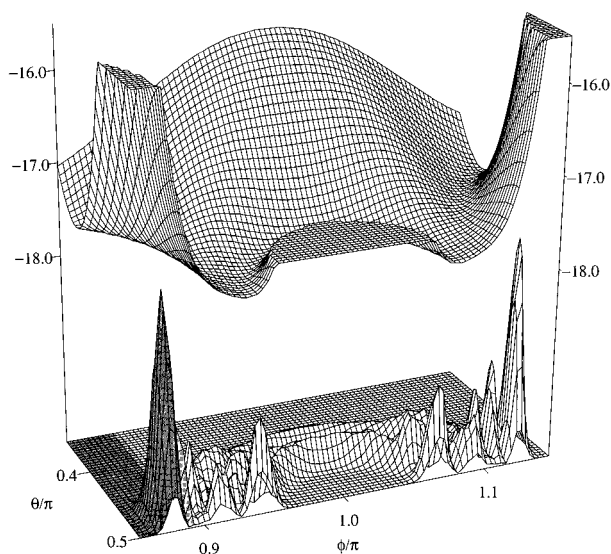
FIG. 12. Lower plot, same as Fig. 11, except that the collision time is now 90 fs, and the $\rho$ value has reached 3.03 Å. The comparison with Fig. 11 shows that during a time interval of 10 fs, the H$_2$ molecule has aligned along the Ar–H$_2$ axis, since $\theta=\pi/2$ corresponds to the collinear configurations. A measure of this alignment effect is shown by the probability the system has to be in the gray region; this amounts to 26%. Upper plot, adiabatic electronic ground state potential energy surface on which the adiabatic wave packet evolves. Energy is in eV.

mation, it keeps this distribution on the first two adiabatic electronic states throughout the transition zone. On the other hand, a system prepared in the Ar$^+$($J=1/2$)+H$_2$($v=0$) state is initially found in the first excited adiabatic electronic state for $r_{H-H}<0.81$ Å and in the second excited adiabatic electronic state for $r_{H-H}>0.81$ Å. It will then barely be found in the adiabatic ground electronic state. This explains the strong difference in the behavior of the two spin orbit states in the transition zone (Fig. 8) at the highest energies considered, and consequently the difference in the reactivity of the Ar$^+$(3/2,1/2)+H$_2$ and the Ar$^+$(1/2,1/2)+H$_2$ states.
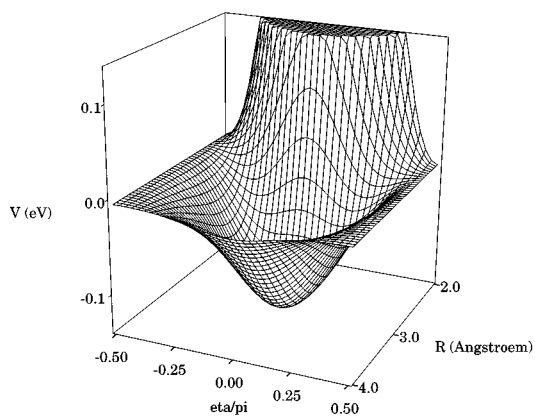


FIG. 13. Dependence on the Jacobi angle $\eta$ of the energy of the vibronic state correlated with the Ar$^+$(3/2 1/2)+H$_2$ relative to its $\eta=0$ value. At large and moderate internuclear distances, the collinear geometry $\eta=0$ is energetically most favorable; at small distances, steric effects tend to favor the perpendicular geometry.
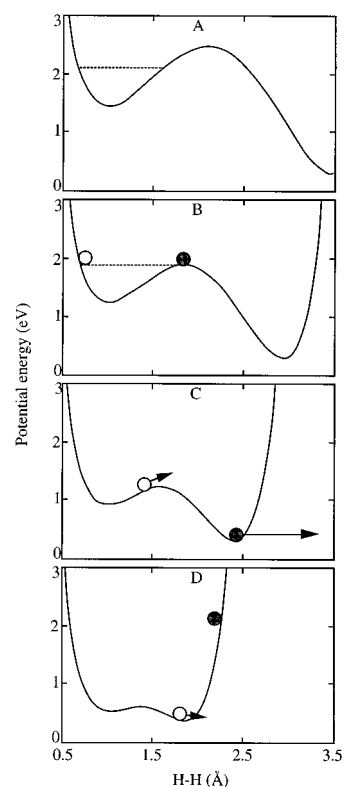


FIG. 14. Qualitative explanation of the existence of a bimodal energy distribution. The figure show cuts of the ground adiabatic potential energy surface in collinear geometry, when Ar approaches H$_2$. In frame A, Ar is far from H$_2$ (Ar–H=5 Å). The molecule classically oscillates in the H$_2$ potential well; its energy is represented by a dashed line. At a given time, the ArH$^+$ well becomes energetically accessible, as shown in frame B corresponding to Ar–H=4.5 Å. The subsequent time evolution strongly depends on the collision velocity. In the considered case, a classical system located at the outer turning point in frame B (gray ball) will gain roughly all the energy of the ArH$^+$ potential well displayed in B. Indeed, the changes of the potential occurring when moving to frame C (Ar–H=4 Å) and then D (Ar–H =3.5 Å) roughly consist in changing the relative position of the two potential wells. This does not affect the gray ball as soon as it leaves the barrier region. Conversely, the time evolution of a classical system lying in B at the inner turning point of H$_2$ does not lead to such an energy gain, because the ArH well has almost completely disappeared when the system reaches the top of the barrier. When the (ArH$_2^+$) system reaches its turning point at a time corresponding to frame D, the gray system has gained energy, and the white system has lost energy.

## B. The reaction

The reaction itself takes place on the ground adiabatic potential energy surface. It can be considered to begin after the transition zone A, namely at values of $\rho$ around 4–4.5 Å. At this point, one should not make the distinction between collisions starting from the ($J=3/2 M_J=1/2$) or the ($J=1/2 M_J=1/2$) states, since in the zone where the reaction takes place, the adiabatic ground state is a mixture of these two states, and more generally of a number of strongly coupled diabatic states. The initial state plays a central role in the preceding part of the collision only (Sec. VI A). At the beginning of the reaction itself, the memory of the initial state lies mainly in the probability amplitude to be in given vibrational states of the electronic adiabatic ground state.
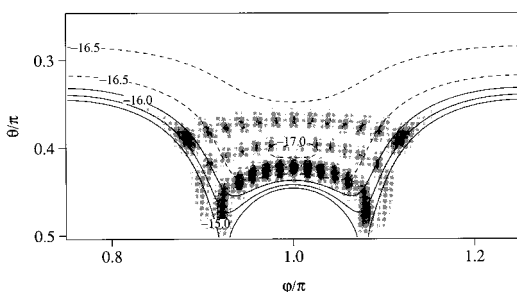
FIG. 15. Probability density of the ground adiabatic wave packet (gray levels) and adiabatic electronic ground state potential in eV (contour lines). The collision starts at $\rho=10$ Å with a collision energy $E=3.0$ eV; the system is initially in the Ar$^+$($J=3/2$ $M_J=1/2$)+H$_2$($^1\Sigma_g$) state. After 33 fs, it has reached the value $\rho=2.27$ Å, where this picture has been drawn. By comparing this view with that of Fig. 12, one sees that the alignment of the H$_2$ molecular axis along the Ar–H$_2$ collision axis does not have the time to take place.

The two initial states also differ by one or two quanta in those vibrational energy levels of the electronic ground adiabatic state at the entrance of the reaction zone. This actually does not make a large difference in the reaction dynamics. On the other hand, the reaction dynamics strongly depends on the collision energy. Indeed, as will be illustrated in the two examples given below, three mechanisms contribute to the reaction; a direct mechanism,[40] where the H atom of the ArH$^+$ molecule was initially pointing towards the Ar$^+$ ion; a knockout mechanism,[40] where a first collision between Ar and one of the H ejects this H atom with a large amount of energy, and leaves the ArH$^+$ molecule with small internal energy; a pop-out mechanism[41] where one of the H atoms is first jammed in a collinear geometry between the Ar atom and the other H atom, and then ejected.

The first example corresponds to collisions starting from Ar$^+$($J=3/2 M_J=1/2$)+H$_2$($^1\Sigma_g$), at a center-of-mass collision energy $E=0.3$ eV. In such a case a non negligible part of the population is found in closed channels, making the vibrational distribution of the ArH$^+$ products not very reliable. Nevertheless, we find that about one half of the population goes into low lying vibrational levels, and one half into high vibrational levels. We may trace back the origin of this phenomenon as follows. According to Sec. VI A, after the intermediate zone A ($t=80$ fs, $\rho=4.24$ Å) the system is in the electronic adiabatic ground state, mainly in the vibrational state $v=2$. During the first ten femtoseconds of its adiabatic life, it tends to adopt a collinear geometry (Fig. 12). At the turning point of the collision, a significant part of the system is in a nearly collinear geometry. The reason for this alignment is that the coupling between the Ar$^+$+H$_2$($^1\Sigma_g$) states and the charge exchange Ar+H$_2^+$ state is—at least asymptotically—proportional to $\cos(\eta_1)$, where $\eta_1$ is the Jacobi angle in the Ar+H$_2$ arrangement. This angular dependence of the coupling results in a well in the ground adiabatic surface in collinear geometry (Fig. 13). Besides the alignment effect, one notes on Fig. 12 that the part of the wave packet lying near the outer vibrational turning point of
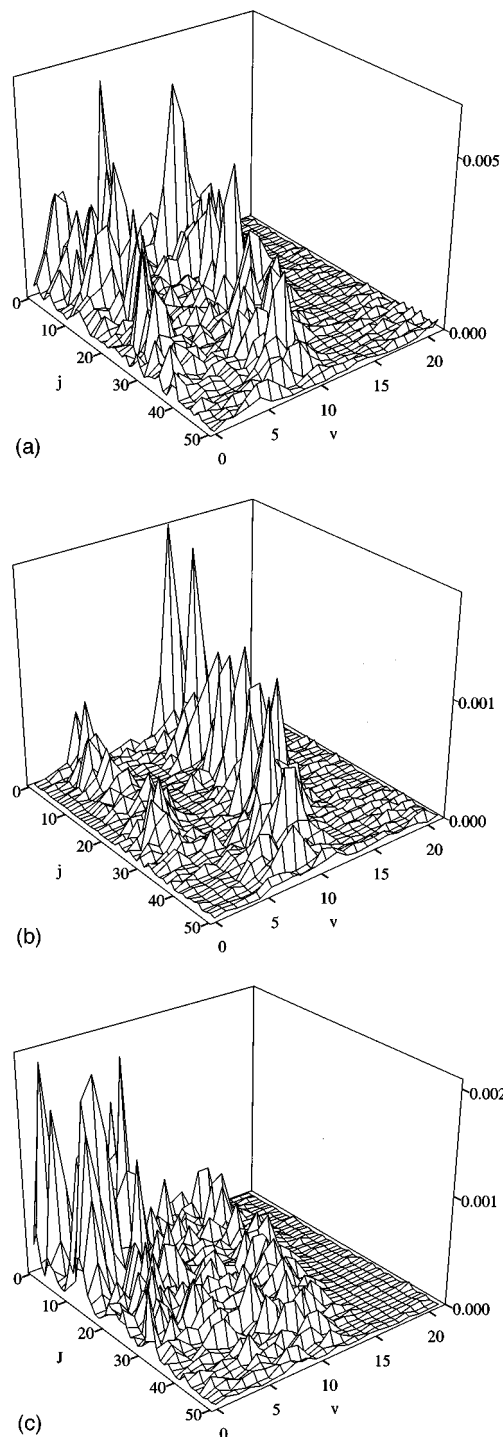


FIG. 16. Frame (a), final rovibrational distribution of the ArH$^+$ molecule as produced by a collision starting from the Ar$^+$($J=3/2$ $M_J=1/2$) level with an energy of 3.0 eV. This distribution exhibits a double structure, which can be attributed to two different mechanisms. The direct mechanism, occurring when the ArH$^+$ molecule is formed with the H atom initially pointing towards the Ar$^+$ ion, leads to the high energy component (frame b), while the knock-out mechanism, occurring when the nearest of the H atoms is ejected by a collision with the Ar$^+$ ion, is responsible for the formation of cold ArH$^+$ molecules (frame c).

H$_2$ in collinear geometry has a potential energy of about 1.5 eV, that is much larger than in the rest of the wave packet. A simple interpretation of this phenomenon is provided in Fig. 14. This localization of the energy in one region of the wave

packet is responsible for the partition of the vibrational distribution into two energy components. This is verified by removing at $t=90$ fs all of the wave packet except a small part lying near the collinear configuration Ar–H$_a$–H$_b$, at the external vibrational turning point of the H$_2$ molecule (see Fig. 12). The cut-off function has been chosen smooth enough to avoid creating spurious high kinetic energy components. At the end of the collision, this part of the wave-packet gives rise to strongly excited vibrational states of ArH$^+$. Moreover, it is observed that the formation of the ArH$_b^+$ molecule (pop-out mechanism) is three times more probable than the formation of the ArH$_a^+$ molecule (direct mechanism). This ratio has a simple explanation; starting from the situation depicted in Fig. 12, the system has to perform a U-turn to go out in the Ar–H$_a$ valley. It is easier for the system to go in the H$_2$ valley, gain a strong H$_2$ rotational energy, be reflected at the $\theta=\pi/2$ axis into the collinear Ar–H$_b$–H$_a$ configuration, and then escape in the Ar–H$_b$ valley. This pop-out mechanism requires that (i) the collision is nearly collinear and that (ii) the translational energy is large. Because none of these two conditions are fulfilled at the beginning of the collision presented here, it is somewhat surprising to observe this effect. It actually happens because the ground adiabatic potential energy surface presents two characteristics; it is attractive (Fig. 4), and its anisotropy favors the collinear geometry (Fig. 13). This transforms a non-collinear low energy collision in the asymptotic zone in a collinear energetic collision in the inner zone.

The second example, also starts from the Ar$^+$($J=3/2$ $M_J=1/2$)+H$_2$($^1\Sigma_g$) state but with a collision energy ten times higher ($E=3$ eV). Paradoxically, this case does not lead to any pop-out mechanism, although the high energy requirement is better fulfilled than in the preceding example. The pop-out mechanism cannot be observed here because the H$_2$ molecule has not time enough to rotate before the reaction itself (Fig. 15). Still, as in the preceding example, the rovibrational distribution of the ArH$^+$ products of such a collision also exhibits two energy components (Fig. 16). The explanation for this bimodal distribution has been found by removing the part of the wave packet located at values of the hyperangle $\varphi$ less than $\pi$ at the beginning of its "adiabatic life," i.e., just after the above mentioned intermediate zone A. Physically, this means that we consider only the situations where a given H atom, hereafter named H$_a$, is nearer to Ar than the other one, named H$_b$. After propagation of this half wave packet, we find that the system forms both ArH$_a^+$ and ArH$_b^+$ molecules, but with a very different internal energy (Fig. 16); the ArH$_a^+$ molecules are much more excited than the ArH$_b^+$ molecules. A simple picture can help understanding this effect. As the translational energy is greater than the internal energy, one can think of the collision in an impulsive picture. Within this frame, the spectator stripping model assumes that the Ar atom collides only with the nearest H atom; on the contrary, the knock-out mechanism assumes that a first collision with the H$_a$ atom ejects this atom, and leaves the system in the Ar–H$_b^+$+H$_a$ state. These two simple models lead to very different predictions of the internal energy of the molecule, since the knock out mechanism allows

the Ar atom to give a large part of its energy to the ejected H$_a$ atom and leads to low energy ArH$_b^+$ molecules, what the spectator stripping model does not allow.

## VIII. CONCLUSION

From a technical point of view, we have shown that the semiclassical coupled wave packet approach in hyperspherical coordinates enables us to describe simultaneously all the events occurring during an Ar$^+$+H$_2$ collision at a state to state level. We have limited on purpose the present study to $\mathscr{J}=0$ in order to show the feasibility of the method and its potency. Extension to the $\mathscr{J}>0$ is straightforward: in the latter case, the number of degrees of freedom is four instead of three,[28(c)] yet the coplanar approximation[42] leads to the same computational effort whatever the value of $\mathscr{J}$ is. Still one should not overlook weaknesses of the method that stem from the use of a common trajectory to describe the classical evolution of the hyperspherical radius. The common turning point this imposes to the whole system may somewhat distort its actual behavior. Yet, the increase of both energy and angular momentum is expected to attenuate this drawback. Another well known defect of the common classical trajectory method is the possible population of closed channels.[36] This aspect will have to be investigated, and hopefully corrected in future applications of the method.

From a physical point of view, we have demonstrated here that the Ar$^+$+H$_2$ reactive collision can be seen as a two step process. In the entrance valley, the coupling becomes so large that the behavior of the system becomes adiabatic in the inner region. The diabatic to adiabatic change of behavior constitutes the first step of the process. The part of the system which goes in the ground adiabatic electronic state can react. The difference in the behavior of the two reactant fine structure states ($J=3/2$, $M_J=1/2$) and ($J=1/2$, $M_J=1/2$) observed experimentally is interpreted by the fact that the (3/2,1/2) diabatic state "correlates" better with the ground adiabatic electronic state than the (1/2,1/2) state does. The second step of the process leading to reaction is the time evolution of the adiabatic uncoupled wavepacket evolving on the ground adiabatic electronic surface. At low energy, we have shown that the effects of the anisotropy of the potential play a crucial role. The H$_2$ molecule first aligns along the Ar$^+$–H$_2$ axis, and is simultaneously accelerated, leading to a pop-out mechanism. This mechanism does not exist at higher energy, because the H$_2$ molecule cannot align before the collision with the Ar atom.

## ACKNOWLEDGMENTS

[1] D. P. Stevenson and D. O. Schissler, J. Chem. Phys. **29**, 282 (1958).

[2] K. M. Ervin and P. B. Armentrout, J. Chem. Phys. **83**, 166 (1985).

[3] (a) C. L. Liao, R. Xu, G. D. Flesch, M. Baer, and C. Y. Ng, J. Chem. Phys. **93**, 4818 (1990); (b) C.-L. Liao, R. Xu, S. Nourbakhsh, G. D. Flesch, M. Baer, and C. Y. Ng, *ibid*. **93**, 4832 (1990).

[4] M. Hawley and M. A. Smith, J. Chem. Phys. **96**, 7440 (1992).

[5] W. A. Chupka and M. E. Russell, J. Chem. Phys. **49**, 5426 (1968).

[6] (a) K. Tanaka, J. Durup, T. Kato, and I. Koyano, J. Chem. Phys. **73**, 586 (1980); (b) **74**, 5561 (1981).

[7] C. J. Latimer and F. M. Campbell, J. Phys. B **15**, 1765 (1982).

[8] T. Kato, J. Chem. Phys. **80**, 6105 (1984).

[9] M. Hamdan, K. Birkinshaw, and N. D. Twiddy, Int. J. Mass Spectrom. Ion Processes **62**, 297 (1984).

[10] G. Henri, M. Lavollée, O. Dutuit, J. B. Ozenne, P. M. Guyon, and E. A. Gislason, J. Chem. Phys. **88**, 6381 (1988).

[11] B. G. Lindsay and C. J. Latimer, J. Phys. B **21**, 1617 (1988).

[12] (a) P. Tosi, F. Boldo, F. Eccher, M. Filippi, and D. Bassi, Chem. Phys. Lett. **164**, 471 (1989); (b) P. Tosi, F. Escher, D. Bassi, F. Pirani, D. Cappelletti, and V. Aquilanti, Phys. Rev. Lett. **67**, 1254 (1991); (c) P. Tosi, O. Dmitrijev, Y. Soldo, D. Bassi, D. Cappelletti, F. Pirani, and V. Aquilanti, J. Chem. Phys. **99**, 985 (1993).

[13] T. F. George and R. J. Suplinskas, J. Chem. Phys. **51**, 3666 (1969).

[14] G. R. North and J. J. Leventhal, J. Chem. Phys. **51**, 4236 (1969).

[15] D. Hyatt and L. Stanton, Chem. Phys. Lett. **10**, 10 (1971).

[16] P. J. Kuntz and A. C. Roach, J. Chem. Soc. Faradey Trans. II **68**, 259 (1972).

[17] E. A. Gislason, J. Chem. Phys. **57**, 3396 (1972).

[18] (a) S. Chapman and R. K. Preston, J. Chem. Phys. **60**, 650 (1974); (b) S. Chapman, *ibid*. **82**, 4033 (1985); (c) S. Chapman, in *State Selected and State to State Ion–Molecule Reaction Dynamics. Part 2: Theory*, edited by M. Baer and C. Y. Ng (Wiley, New York, 1992), pp. 447–452.

[19] (a) M. Baer and J. A. Beswick, Chem. Phys. Lett. **51**, 360 (1977); (b) M. Baer, Mol. Phys. **35**, 1637 (1978); (c) M. Baer and J. A. Beswick, Phys. Rev. A **19**, 1559 (1979).

[20] S. M. McPhail and R. G. Gilbert, Chem. Phys. **34**, 319 (1978).

[21] M. Kimura, S. Chapman, and N. F. Lane, Phys. Rev. A **33**, 1619 (1986).

[22] (a) M. Baer, H. Nakamura, and A. Oshaki, Chem. Phys. Lett. **131**, 468 (1986); (b) M. Baer and H. Nakamura, J. Chem. Phys. **87**, 4651 (1987).

[23] E. A. Gislason and M. Sizun, Chem. Phys. **133**, 237 (1989).

[24] (a) M. Baer, C.-L. Liao, R. Xu, S. Noubarkhsh, G. D. Flesch, M. Baer, C. Y. Ng, and D. Neuhauser, J. Chem. Phys. **93**, 4845 (1990); (b) M. Baer, in *State Selected and State to State Ion–Molecule Reaction Dynamics. Part 2: Theory*, edited by M. Baer and C. Y. Ng (Wiley, New York, 1992), pp. 216–236.

[25] E. A. Gislason and G. Parlant, J. Chem. Phys. **94**, 6598 (1991).

[26] N. Marković, G. Nyman, and S. Nordholm, Chem. Phys. **167**, 157 (1992).

[27] (a) J. T. Muckerman, R. D. Gilbert, and G. D. Billing, J. Chem. Phys. **88**, 4779 (1988); (b) G. D. Billing and J. T. Muckerman, *ibid*. **91**, 6830 (1989); (c) N. Marković, G. D. Billing, and J. T. Muckerman, Chem. Phys. Lett. **172**, 509 (1990).

[28] (a) B. R. Johnson, J. Chem. Phys. **73**, 5051 (1980); (b) **79**, 1906 (1983); (c) **79**, 1916 (1983).

[29] G. D. Billing and N. Marković, J. Chem. Phys. **99**, 2674 (1993).

[30] J. C. Tully, J. Chem. Phys. **59**, 5122 (1973).

[31] E. E. Nikitin, M. Y. Ovchinnikova, and D. V. Shalashilin, Chem. Phys. **111**, 313 (1987).

[32] Strictly speaking, condition (20) can be replaced by the less restrictive condition $\Psi'_{n'}(\theta,\varphi) = e^{i\xi}\Psi_n(\theta, 2\pi - \varphi)$, where $\xi$ does not depend on $\theta$ and $\varphi$.

[33] D. Kosloff and R. Kosloff, J. Comp. Phys. **52**, 35 (1983).

[34] C. Leforestier, R. H. Bisseling, C. Cerjan, M. D. Fett, R. Friesner, A. Guldberg, A. Hammerich, G. Jolicard, W. Karrlein, H.-D. Meyer, N. Lipkin, O. Roncero, and R. Kosloff, J. Comp. Phys. **94**, 59 (1991).

[35] M. Gilibert, I. Last, A. Baram, and M. Baer, Chem. Phys. Lett. **221**, 327 (1994).

[36] H.-D. Meyer and W. H. Miller, J. Chem. Phys. **70**, 3214 (1979).

[37] P. M. Hierl, V. Pacăk, and Z. Herman, J. Chem. Phys. **67**, 2678 (1977).

[38] T. Nakamura, N. Kobayashi, and Y. Kaneko, J. Phys. Soc. Jpn. **55**, 3831 (1986).

[39] F. Aguillon, V. Sidis, and J. P. Gauyacq, Mol. Phys. **81**, 169 (1994).

[40] B. H. Mahan, W. E. W. Ruska, and J. S. Winn, J. Chem. Phys. **65**, 3888 (1976); S. A. Safron, J. Phys. Chem. **89**, 5713 (1985).

[41] M. Sizun, G. Parlant, and E. A. Gislason, Chem. Phys. Lett. **139**, 1 (1987).

[42] N. Marković and G. D. Billing, Chem. Phys. **173**, 385 (1993).